Cell

Mechanism of Local and Global Ca^{2+} Sensing by Calmodulin in Complex with a Ca^{2+} Channel

Michael R. Tadross,[1] Ivy E. Dick,[1] and David T. Yue[1,*]
[1]Calcium Signals Laboratory, Departments of Biomedical Engineering and Neuroscience, The Johns Hopkins University School of Medicine, Ross Building, Room 713, 720 Rutland Avenue, Baltimore, MD 21205, USA
*Correspondence: dyue@bme.jhu.edu
DOI 10.1016/j.cell.2008.05.025

SUMMARY

Calmodulin (CaM) in complex with Ca^{2+} channels constitutes a prototype for Ca^{2+} sensors that are intimately colocalized with Ca^{2+} sources. The C-lobe of CaM senses local, large Ca^{2+} oscillations due to Ca^{2+} influx from the host channel, and the N-lobe senses global, albeit diminutive Ca^{2+} changes arising from distant sources. Though biologically essential, the mechanism underlying global Ca^{2+} sensing has remained unknown. Here, we advance a theory of how global selectivity arises, and we experimentally validate this proposal with methodologies enabling millisecond control of Ca^{2+} oscillations seen by the CaM/channel complex. We find that global selectivity arises from rapid Ca^{2+} release from CaM combined with greater affinity of the channel for Ca^{2+}-free versus Ca^{2+}-bound CaM. The emergence of complex decoding properties from the juxtaposition of common elements, and the techniques developed herein, promise generalization to numerous molecules residing near Ca^{2+} sources.

INTRODUCTION

Ca^{2+} constitutes a ubiquitous signal with wide-ranging biological impact (Berridge et al., 2000). Despite the pervasive nature of Ca^{2+}, its detection can be highly selective in space and time, as required for specificity in signaling to appropriate targets (Bootman et al., 2001; Cullen, 2006; De Koninck and Schulman, 1998; Dolmetsch et al., 1998; Gu and Spitzer, 1995; Li et al., 1998; Oancea and Meyer, 1998; Winslow and Crabtree, 2005). Among the most critical of these detection modes are those relating to Ca^{2+} sensors positioned in close proximity, i.e., within nanometers, of Ca^{2+} sources. This placement of sensors within such a "nanodomain" promotes rapid and privileged Ca^{2+} signaling (Augustine et al., 2003; Bootman et al., 2001; Catterall, 1999). However, such proximity to a Ca^{2+} source challenges a sensor's ability to integrate Ca^{2+} signals from distant sources, which is essential for coordinated signaling at the whole-cell level.

A prototype for coupled sensors and sources is the Ca^{2+} sensor calmodulin (CaM), in its regulation of the Ca_V1-2 family of Ca^{2+} channels (Dunlap, 2007). CaM is continuously complexed with channels as a resident Ca^{2+} sensor (Erickson et al., 2001; Pitt et al., 2001), and Ca^{2+} binding to the C- and N-terminal lobes of CaM can each induce a separate form of regulation on the same channel (DeMaria et al., 2001; Yang et al., 2006). Given the approximate diameter of Ca^{2+} channels (Wang et al., 2002), the resident CaM would be ~10 nm from the channel pore, well within the channel nanodomain. Despite this proximity, each lobe responds selectively to distinct Ca^{2+} signals (cartooned in Figure 1A), which differ in both their spatial distribution (top row) and temporal characteristics (bottom row). Under physiological conditions, the composite Ca^{2+} signal (Figure 1A, left column) is the sum of two distinct components. First, Ca^{2+} inflow during channel openings produces a "local signal" component (Figure 1A, middle column) comprising brief yet intense local spikes of amplitude Ca_{spike} ~100 μM (bottom row). These spikes are tightly synchronized with openings of the host channel, and localized to the nanodomain (top row, green hemisphere) (Neher, 1998; Sherman et al., 1990) (see Supplemental Data [3], available online). Second, accumulation of Ca^{2+} from distant sources (e.g., other Ca^{2+} channels) generates a "global signal" component (Figure 1A, right column) consisting of a far smaller (~5 μM) global pedestal (bottom row), which is spatially widespread (top row, green shading). In the Ca_V1-2 family of Ca^{2+} channels, regulation triggered by the C-lobe of CaM exploits channel proximity and responds almost maximally to the local Ca^{2+} signal alone (Liang et al., 2003). This "local selectivity" is schematized for a Ca^{2+}-dependent inactivation process (CDI) triggered by the C-lobe (Figure 1B). Such CDI produces a strong decay of Ca^{2+} current during sustained voltage activation whether Ca^{2+} is buffered at physiological levels, or much more strongly (Figure 1B). Since high Ca^{2+} buffering eliminates the global pedestal while hardly affecting local spikes (Figure 1A, middle column; Supplemental Data [3]) (Neher, 1998), the sparing of CDI under this condition indicates that the local signal alone is sufficient. By contrast, N-lobe mediated regulation of all Ca_V2 channels somehow prefers the diminutive global pedestal over the far larger local spikes. The hallmark of this "global selectivity" is the presence of strong CDI in physiological buffering (Figure 1C, left), and its near absence in high buffering (Figure 1C, middle) (DeMaria et al., 2001; Liang et al., 2003).

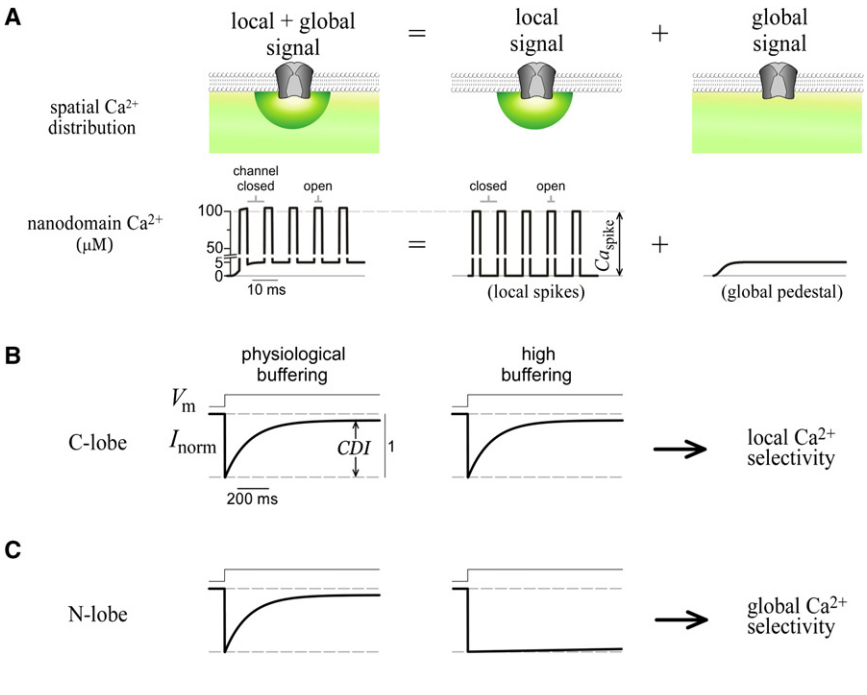

Figure 1. Definition of Spatial Selectivity

(A) Cartoon of Ca^{2+} signals near a channel. Spatial (top row) and temporal (bottom row) profiles are shown. Note axis break in nanodomain Ca^{2+}. Composite signal (left column) is the sum of local (middle column) and global (right column) components.

(B) Schematic of C-lobe CDI, which exemplifies local selectivity. Intracellular buffering conditions cause the Ca^{2+} input signals to correspond to those shown directly above in (A).

(C) Schematic of N-lobe CDI, which exemplifies global selectivity, buffering as in (B).

Without this detection mode, Ca^{2+} feedback would be restricted to isolated complexes, and lack coordination over larger regions. Global selectivity is thus critical to the signaling repertoire of Ca^{2+} sensors positioned near Ca^{2+} sources.

What are the mechanisms for the contrast in spatial Ca^{2+} selectivity of the lobes of CaM? The simplest explanation would presume that while the C-lobe resides within the nanodomain, the N-lobe lies outside this zone, where the local signal would be smaller than the global pedestal (Figure 1A, top row). However, each channel is constitutively complexed with a single CaM (Mori et al., 2004; Yang et al., 2007), and the lobes of CaM are very close to one another (<6 nm), indicating that both lobes are likely within the nanodomain (Dunlap, 2007; Stern, 1992). Hence, the N-lobe must be insensitive to Ca^{2+} intensity, and instead may respond to certain temporal features of nanodomain Ca^{2+} (Figure 1A, bottom row). Though some Ca^{2+}-dependent mechanisms that favor specific temporal patterns of Ca^{2+} have been characterized (De Koninck and Schulman, 1998; Oancea and Meyer, 1998), none can respond to signals of low amplitude and frequency (global pedestal), while ignoring signals of high amplitude and frequency (local spikes). Hence, global selectivity must employ a thus far unknown mechanism.

Here, theoretical and experimental advances explain how this unusual selectivity for global Ca^{2+} signals arises from the combination of two common elements: rapid Ca^{2+} release from CaM, together with greater channel affinity for Ca^{2+}-free (apoCaM) versus Ca^{2+}-bound CaM (Ca^{2+}/CaM). Since our proposed mechanism requires CaM/channel interactions as present within intact channels, we develop the means to probe Ca^{2+} dynamics within this integrated setting, using channels engineered for enhanced opening, with a "voltage block" electrophysiological technique to precisely control nanodomain Ca^{2+}. These tools resolve Ca^{2+} response characteristics clearly distinctive of the proposed mechanism. Combining this approach with manipulation of a recently identified CaM regulatory site (Dick et al., 2008) enables quantitative confirmation of a key prediction—selectivity can be incrementally changed from global to local by adjusting the ratio of channel affinity for apoCaM versus Ca^{2+}/CaM. Our findings generalize across Ca_V1–Ca_V2 channels, and likely extend to diverse Ca^{2+} sensors situated near Ca^{2+} sources.

RESULTS

Dominant Conformations of the CaM/Channel Complex Involved in Ca^{2+} Sensing

To explore how the CaM/channel complex could produce both local and global Ca^{2+} selectivity, we outlined a basic system comprised of the dominant conformations of this molecular assembly (Figure 2A). Several established features were considered. First, a 1:1 CaM/channel stoichiometry has been demonstrated (Mori et al., 2004; Yang et al., 2007). Second, two distinct types of CaM/channel interactions are known to exist: apoCaM binding, which anchors CaM to the channel as a resident sensor; and Ca^{2+}/CaM binding, which here produces CDI. Finally, an appropriate first-order approximation was to separately consider the operation of the C- and N-lobes of CaM, each with simultaneous (un)binding of two Ca^{2+} ions (Linse et al., 1991; Martin et al., 1985). This single-lobe approximation was reinforced in our experiments by the use of mutant CaM molecules that restrict Ca^{2+} binding to one lobe or the other (DeMaria et al., 2001; Peterson et al., 1999). Based upon these features, four main conformations result (Figure 2A, valid for either the C- or N-lobe). State 1 represents apoCaM (yellow circle) bound to the channel preassociation site (round pocket). Direct Ca^{2+} binding to CaM in state 1 is not considered, as such interaction is unlikely according to an analogous apoCaM/peptide structure (Houdusse et al., 2006). State 2 portrays apoCaM after it releases from the preassociation site, at which point it can bind Ca^{2+} to produce Ca^{2+}/CaM (square) in state 3. We reason that a transiently dissociated lobe of CaM (state 2 or 3) does not diffuse away (retained within a channel alcove), because of the slow

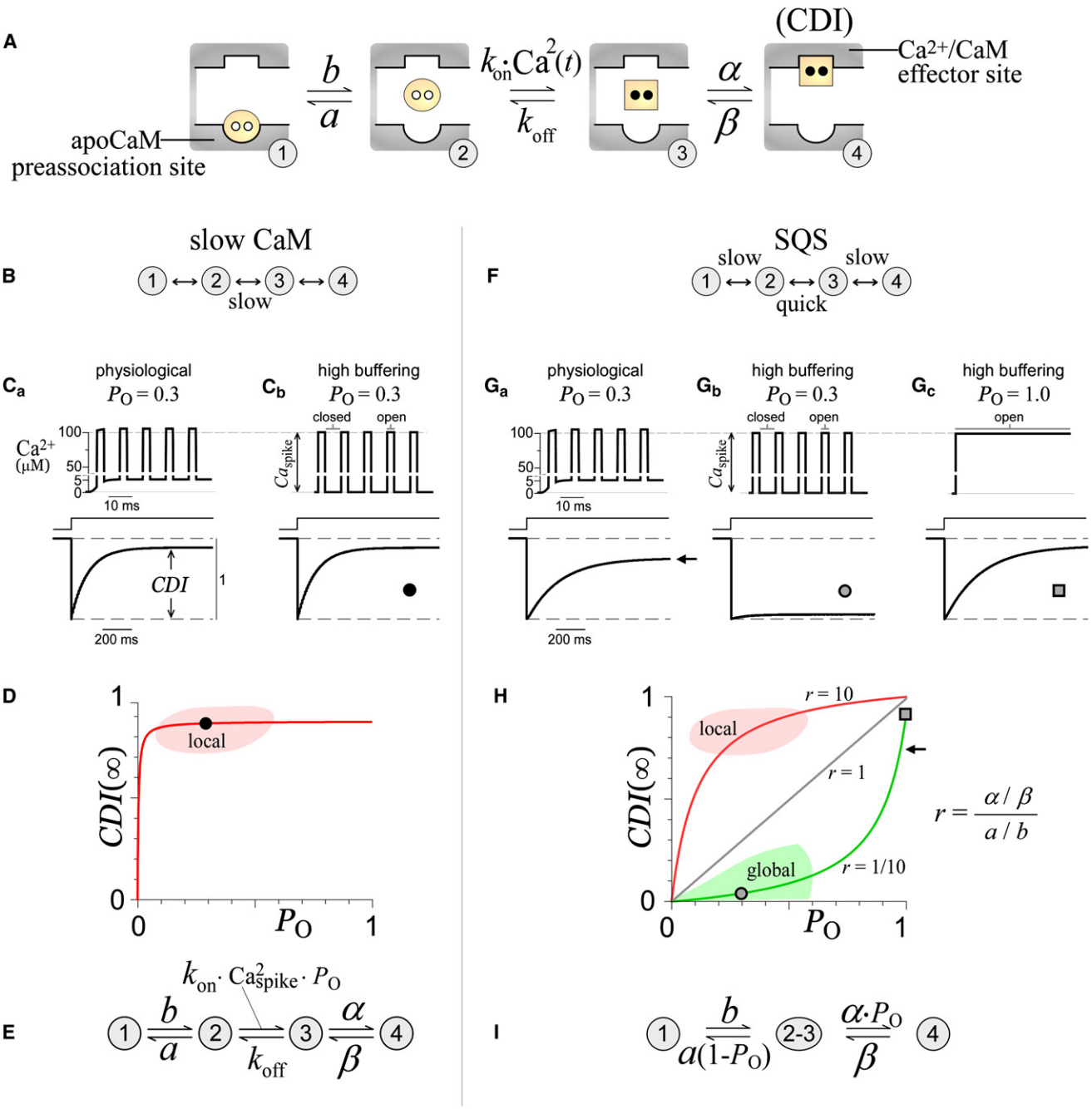

Figure 2. Ca^{2+} Decoding Mechanisms for the CaM/Channel Complex

(A) Basic states for a lobe of CaM in complex with a Ca^{2+} channel. In state 1, apoCaM (yellow circle) is bound to the apoCaM site (round pocket). In state 2, apoCaM is a transiently dissociated. In state 3, CaM binds two Ca^{2+} ions (black dots) to become Ca^{2+}/CaM (yellow square), which can then bind the Ca^{2+}/CaM effector site (square pocket), yielding CDI (state 4).

(B) Slow CaM mechanism, configurations of the basic system where switching between states 2 and 3 is slow relative to channel gating.

(C) Slow CaM numerical simulations exhibit local selectivity. Ca^{2+} signals (top) are given as input. Note Ca^{2+} axis break in panels (C) and (G). Parameters (in ms^{-1}) $\alpha = 0.5$, $\beta = 0.05$, $a = 60$, $b = 0.04$, $k_{off} = 0.003$, and $k_{on} = 1.2 \times 10^{10}$ M^{-2} ms^{-1}. See Experimental Procedures for simulation details.

(D) Slow CaM $CDI(\infty)$–P_O relations exhibit local Ca^{2+} selectivity. Round symbol corresponds to simulation in (C_b). Red curve corresponds to Equation 1, with parameters as in (C).

(E) Equivalent slow-CaM mechanism (see Supplemental Data [2]).

(F) SQS mechanism has slow state 1-2 and state 3-4 switching, and quick state 2-3 switching, all relative to channel gating.

(G) SQS numerical simulations exhibiting global selectivity. Parameters (in ms^{-1}) $\alpha = 0.1$, $\beta = 0.01$, $a = 0.4$, $b = 0.004$, $k_{off} = 3$, and $k_{on} = 3.7 \times 10^{12}$ $M^{-2}ms^{-1}$ (see Experimental Procedures).

rate of exchange between perfused CaM and channel-associated CaM (Chaudhuri et al., 2005). Finally, in state 4, Ca^{2+}/CaM binds the channel effector site (square pocket), which triggers CDI. The effector site is unlikely to bind apoCaM, because CDI is absent without Ca^{2+}. Further arguments in support of this basic four-state configuration appear in the Discussion and Supplemental Data (1F).

Hypothesis for Local Ca^{2+} Sensing by the C-Lobe of CaM

How might local Ca^{2+} selectivity of the C-lobe arise? This lobe is known to release Ca^{2+} slowly compared to the millisecond duration of Ca^{2+} channel closings (Bayley et al., 1984; Black et al., 2005; Chaudhuri et al., 2007; Imredy and Yue, 1994; Martin et al., 1985), yielding a "slow CaM" mechanism (Figure 2B). Given this scheme, numerical simulations readily exhibit local selectivity, with strong CDI produced by Ca^{2+} signals appropriate for both physiological Ca^{2+} buffering (Figure 2C_a) and high buffering (Figure 2C_b, see legend for simulation details). This outcome is plausible because once CaM binds Ca^{2+} during a channel opening (Figure 2A, state 3), CaM will likely retain Ca^{2+} during millisecond closures, causing accumulation in state 3 that subsequently drives entry into state 4 (CDI) (Supplemental Data [2]).

For analytical insight, we define a graphical "input-output" relation for Ca^{2+} detection (Figure 2D). The "output" is taken as the extent of CDI reached at steady-state ($CDI(\infty)$), and the "input" as the channel open probability P_O, both as observed under high Ca^{2+} buffering. In this regime, P_O specifies the fraction of time Ca^{2+} is present (the "fractional presence" of Ca^{2+}). This quantity is useful because nanodomain Ca^{2+} will achieve a steady concentration of Ca_{spike} within microseconds of channel opening, and rapidly decay to zero upon channel closing (Figure 2C_b, top; Supplemental Data [3]) (Sherman et al., 1990) . Accordingly, P_O becomes directly proportional to Ca^{2+} entry, and thereby serves as shorthand for the Ca^{2+} input. A first beneficial outcome of this format is a visual definition of local Ca^{2+} selectivity. Specifically, local selectivity maintains near maximal CDI under high buffering, with inputs spanning the range of naturally occurring P_O (~0.1–0.6). Therefore, the $CDI(\infty)$–P_O relation for all processes with local selectivity must intersect the red zone in Figure 2D, as exemplified by the data point (round symbol) corresponding to our numerical simulation (Figure 2C_b). As a second advantage, we deduce a simple formula for the $CDI(\infty)$–P_O response of the slow CaM mechanism. Under high buffering, slow Ca^{2+} release from the C-lobe allows the time-varying rate constant for transitions from state 2 to 3 ($= k_{on} \cdot Ca^2(t)$) to be replaced by a fixed value equal to $k_{on} \cdot Ca_{spike}^2 \cdot P_O$ (Supplemental Data [2A]). This yields the equivalent system in Figure 2E, from which algebraic manipulation gives the analytic $CDI(\infty)$–P_O relation, with $CDI(\infty)$ proportional to steady-state occupancy of state 4.

$$CDI(\infty) = G \cdot \frac{P_O}{P_O + K_{eff}}. \qquad \text{(Equation 1)}$$

This relation resembles the Michaelis-Menton equation, with P_O analogous to substrate concentration. G incorporates the affinity of the channel for the Ca^{2+}-bound C-lobe, and K_{eff} reflects the balance between Ca_{spike} and CaM affinity for Ca^{2+} (Supplemental Data [2B]). Though Equation 1 is defined for high buffering, the strong CDI characteristic of Ca^{2+}-detection processes under physiological Ca^{2+} buffering constrains $G \sim 1$ and $K_{eff} \ll 1$ (Supplemental Data [2C]). Hence, any slow CaM mechanism will invariably produce local selectivity, with saturating $CDI(\infty)$–P_O relations that intersect the red zone (Figure 2D, smooth curve).

Hypothesis for Ca^{2+} Sensing by the N-Lobe of CaM

How might global Ca^{2+} selectivity of the N-lobe arise? For this lobe, Ca^{2+} binding and unbinding should be rapid enough to achieve steady state within the millisecond durations of channel openings and closings (Bayley et al., 1984; Black et al., 2005; Chaudhuri et al., 2007; Imredy and Yue, 1994; Martin et al., 1985). Thus, the system would switch "quickly" between states 3 and 2, in sync with channel openings and closings. A second difference from the C-lobe regime is that the kinetics of entry and exit from the outermost states become important. Switching between states 3 and 4 must be "slow" because experimentally, both CDI onset and recovery take much longer than milliseconds (Schnee and Ricci, 2003). If switching between states 1 and 2 is similarly slow, the resulting SQS mechanism ("slow *q*uick slow" in Figure 2F) can produce global selectivity—simulated CDI is strong under physiological buffering (Figure 2G_a), but absent in high buffering (Figure 2G_b and legend). A more quantitative definition of the kinetic constraints for the SQS regime appears in Supplemental Data (1A).

This mechanism achieves global selectivity by combining two factors which collaborate to resist inactivation in response to transient and high-amplitude local Ca^{2+} spikes. Consider the case where only local spikes are present, such as in high buffering (Figure 2G_b, top). First, since the preassociated form of apoCaM (Figure 2A, state 1) binds Ca^{2+} poorly, the long lifetimes in state 1 can "protect" CaM from binding Ca^{2+} during brief Ca^{2+} spikes of high intensity. Second, should this first line of protection fail and state 3 be reached, rapid Ca^{2+} release ensures prompt return to state 2 during channel closures, thus preventing CDI (state 4) and favoring return to the apoCaM preassociated site (state 1). Under physiological buffering, however, global signals would bypass both protective measures. The persistence of a ~5 μM global Ca^{2+} pedestal (Figure 2G_a, top), whose amplitude exceeds the micromolar Ca^{2+} affinity of the N-lobe, would outlast lifetimes in protected state 1 (Figure 2A) and subsequently allow state 2 to bind Ca^{2+} and accumulate in state 3, thus driving strong CDI (state 4). Likewise, even under high buffering, if a channel had a P_O of 1, the continuous local Ca^{2+} entry would produce a ~100 μM Ca^{2+} pedestal (Figure 2G_c, top). This sustained Ca^{2+} signal would again overwhelm both measures of

(H) SQS $CDI(\infty)$–P_O relations exhibit global or local selectivity. Symbols (circle, square, and arrow) correspond to simulations in (G). Green curve corresponds to Equation 2, with parameters as in (G). Gray and red curves demonstrate that increasing r, the ratio of channel affinity for Ca^{2+}/CaM versus apoCaM, induces a shift from global to local selectivity.

(I) Equivalent SQS mechanism (see Supplemental Data [1]).

protection, resulting in strong CDI (bottom). This CDI is only slightly stronger than seen at the native channel P_O under physiological buffering (compare Figures 2G$_c$ and 2G$_a$), illustrating that the SQS mechanism is relatively insensitive to Ca^{2+} intensity. Instead, the contrast in CDI produced by different P_O values under high buffering (compare Figures 2G$_b$ and 2G$_c$) implicates a striking preference for the fractional presence of Ca^{2+}.

Viewing these events in the graphical $CDI(\infty)$–P_O format aids analytical understanding of this mechanism (Figure 2H). For orientation, the red zone associated with local selectivity is reproduced from Figure 2D. Additionally, a corresponding green zone for global Ca^{2+} selectivity can be specified, because all processes with global Ca^{2+} selectivity, regardless of mechanism, must exhibit near elimination of CDI by high Ca^{2+} buffering. Indeed, mapping the high-buffering SQS simulation (Figure 2G$_b$) onto this graph (Figure 2H, round symbol) confirms the ability of the SQS mechanism to intersect this global zone (Figure 2H, green shading). This graphical framework motivates deduction of the closed-form $CDI(\infty)$–P_O solution, obtained as follows (Supplemental Data [1A]). Because multiple transitions will occur between states 2 and 3 before exiting to either state 1 or 4, a number of simplifications can be made according to the analysis of Neher and Steinbach (Neher and Steinbach, 1978). States 2 and 3 may be combined into a single state "2-3," with all rate constants replaced by time-independent equivalents (Figure 2I). Since transitions to state 4 can only occur from state 3, which is only occupied during channel openings, the rate constant from compound state "2-3" to state 4 becomes $\alpha \cdot P_O$. Similarly, the rate constant from compound state "2-3" to state 1 is $a \cdot (1 - P_O)$. This equivalent system (Figure 2I) yields:

$$CDI(\infty) = CDI_{max} \cdot \frac{P_O \cdot r}{P_O \cdot (r-1) + 1/\varepsilon + 1} \qquad \text{(Equation 2)}$$

with individual rate constants (a, b, α, β) defined in Figure 2A, $\gamma = \alpha / \beta$, $\varepsilon = a / b$, and $r = \gamma / \varepsilon$. CDI_{max} accounts for the small P_O of inactivated channels (Imredy and Yue, 1994).

Importantly, Equation 2 suggests that the SQS mechanism need not always produce a global Ca^{2+} selectivity. Rather, N-lobe selectivity is predicted to be transformable between global and local extremes by adjusting the ratio of channel affinity for Ca^{2+}/CaM versus apoCaM (parameter r). To begin, we note that CDI at $P_O = 1$ (square in Figures 2G$_c$ and 2H) will always exceed the strong CDI present in physiological buffering (arrow in Figures 2G$_a$ and 2H). This is true because the Ca^{2+} input from a channel with $P_O = 1$ under high buffering (Figure 2G$_c$, top) is larger than the input from a channel with native P_O under physiological buffering (Figure 2G$_a$, top). Hence, we need only consider parameters yielding $CDI(\infty)$–P_O relations with strong CDI at $P_O = 1$. Given this constraint, we first evaluate the case where $r = 1/10$ in Equation 2, as for the simulations in Figure 2G. Here, the equation produces a $CDI(\infty)$–P_O relation that intersects the global zone, as well as the numerically simulated data points (Figure 2H, green curve). Because $r < 1$, the denominator of Equation 2 now differs from a Michaelis-Menton relation. This yields an upward curvature indicating high sensitivity to the fractional presence of Ca^{2+}, as represented by P_O. However, this is not the only mode of operation. Setting $r = 10$ yields a saturating relation that intersects the local selectivity region (Figure 2H, red curve). Finally, if $r = 1$, the relationship becomes a straight line, suggesting that spatial Ca^{2+} preference need not be categorized as strictly local or global (Figure 2H). In fact, the parameter r represents a bias which competes against the two measures of protection described above. If $r < 1$, with apoCaM binding stronger than Ca^{2+}/CaM binding, the protective measures prevail, and a global selectivity results. By contrast, if $r > 1$, the protective measures are overpowered, and a local profile arises.

Stochastic View of Ca^{2+} Sensing in the Nanodomain of a Ca^{2+} Channel

To obtain analytic solutions, we have thus far used "continuum" equations, where the nanodomain Ca^{2+} concentration at every open channel (Figure 2G$_b$, Ca_{spike}) is considered identical. This continuum view has often been used to model Ca^{2+} dynamics in the channel nanodomain (Naraghi and Neher, 1997; Neher, 1998; Sherman et al., 1990; Stern, 1992). However, given the small volume of a nanodomain (~20 nm hemisphere approximating the CaM/channel complex (Wang et al., 2002)), an average of only ~1 Ca^{2+} ion would be present during channel openings. While this corresponds to a large average Ca^{2+} concentration of ~100 μM, the actual integer number of nanodomain Ca^{2+} ions would differ considerably from one CaM/channel complex to the next, raising concerns with the continuum equations. To validate the continuum derivations of the slow CaM and SQS mechanisms, we used MCell algorithms (Stiles and Bartol, 2001) to stochastically simulate individual Ca^{2+} ions as they diffuse and interact with the CaM/channel complex (Supplemental Data [3] and Movie S1). These stochastic simulations fully confirm Equations 1 and 2. The main factor reconciling continuum and stochastic outcomes is the large flux of Ca^{2+} ions through an open channel (>2000 per millisecond). When viewed over the millisecond timescale of channel gating, every CaM/channel complex samples essentially the same large number of Ca^{2+} ions passing through the nanodomain. Thus, despite differences in the number of Ca^{2+} ions at a given instant of time, the continuum equations remain appropriate.

Experimental Predictions for Candidate Mechanisms of Ca^{2+} Decoding

The core predictions of these Ca^{2+} sensing schemes are:

(1) For C-lobe regulation, the slow CaM mechanism (Figure 2B) predicts that $CDI(\infty)$–P_O relations should follow a saturating Michaelis-Menton profile (Equation 1, Figure 2D).

For N-lobe regulation, two predictions would confirm the SQS mechanism (Figure 2F).

(2) N-lobe processes need not always exhibit global Ca^{2+} selectivity, and adjusting the ratio of channel affinities for Ca^{2+}/CaM to apoCaM (parameter r) should incrementally transform spatial selectivity between global and local extremes (Figure 2H). In particular, the value of r, as determined from fits of electrophysiological data with Equation

2, should be linearly related to the actual ratio of channel binding affinities for Ca^{2+}/CaM relative to apoCaM.

(3) N-lobe $CDI(\infty)$–P_O relationships should match Equation 2 with regard to nuances of shape (Figure 2H). The strongest support for the SQS mechanism would be upward curvature in $CDI(\infty)$–P_O relations with $r < 1$, as this outcome uniquely identifies the SQS mechanism from among a large class of alternatives (Supplemental Data [1]).

Voltage-Block Technique for Experimental Determination of $CDI(\infty)$–P_O Relations

Testing these predictions would require adjustment of channel P_O, while holding unitary current size (and thereby Ca_{spike}) constant. Here, we describe a "voltage block" protocol that enables such P_O adjustability (Figure 3A). A key principle is that the P_O, and thereby the pattern of channel gating, will be identical during depolarizations to either the step potential (top graph, V_U, "unblocked" voltage) or the reversal potential (V_B, "blocked" voltage), so long as both potentials reside on the plateau of the voltage activation curve, drawn with maximal $P_O = P_{O,max}$. At V_U, channel openings would produce single-channel current $i(t)$ (middle row) characterized by $P_O = P_{O,max}$. At V_B, however, there is no driving force for Ca^{2+} entry even when the channel is open. Thus, by inserting repetitive blocking sojourns to V_B (bottom row), the same gating pattern (middle row) would produce a lower effective P_O (bottom row). By adjusting the time spent at V_B ($= T_B$) and the time at V_U ($= T_U$), we can freely dial-in this effective P_O according to $P_{O,EFF} = P_{O,max} \cdot T_U/(T_U + T_B)$. $Ca_V1.3$ single-channel records illustrate this paradigm (Figure 3B). The top row shows Ba^{2+} currents without voltage block ($P_{O,EFF} = P_{O,max}$). The middle row illustrates a 40% block ($P_{O,EFF} = 0.6 \cdot P_{O,max}$), and the bottom an 80% block ($P_{O,EFF} = 0.2 \cdot P_{O,max}$).

Testing the Slow CaM Hypothesis by Voltage-Block of C-lobe CDI in $Ca_V1.3$ Channels

We first applied voltage block analysis to $Ca_V1.3$ channels, as they exhibit strong C- and N-lobe mediated forms of CDI (Yang et al., 2006), facilitating tests of both slow CaM and SQS mechanisms in a uniform background. For $P_{O,max}$ calibration, we determined the activation curve from single $Ca_V1.3$ records evoked by voltage ramps (Figure 3C, top). By averaging such records (middle, red trace), and normalizing by the open current level (dashed curve), we specified the activation curve (bottom, red trace). The single-channel result then calibrated whole-cell activation curves (circles, Supplemental Data [4A and 4B]).

To explore the local selectivity of the C-lobe form of CDI in isolation, we coexpressed channels with CaM_{12}, a mutant CaM with selective retention of C-lobe Ca^{2+} binding (DeMaria et al., 2001; Yang et al., 2006). Figure 3D (top row) shows the sharp decay of Ca^{2+} current in the absence of voltage block, where the symbols indicate the precise inactivation time course (Supplemental Data [4C]). With 40% block (middle row), inactivation is hardly changed. Not until ~80% block (bottom row) does inactivation weaken. To account for minor voltage-dependent effects, we normalized inactivation time points in Ca^{2+} (Figure 3D) by those in Ba^{2+} (Figure 3E), yielding the time course of pure CDI (Figure 3F). Plotting the terminal points ($\sim CDI(\infty)$) as a function of $P_{O,EFF}$ yielded the experimentally resolved $CDI(\infty)$–P_O relation in Figure 3G. To obtain a lower-limit estimate of the $P_O = 1$ data point, we used the CDI measured under physiological buffering (Figure 3G, inset). As presented earlier, this is reasonable because the nanodomain Ca^{2+} signal for a channel with $P_O = 1$ under high buffering (Figure 2G_c, top) would be larger than for a channel with native $P_O \approx 0.3$ under physiological buffering (Figure 2G_a, top). The data (Figure 3G) fit well with Equation 1 for the slow CaM mechanism (red curve), thus fulfilling prediction 1.

Testing the SQS Hypothesis by Voltage Block of N-Lobe CDI in $Ca_V1.3$ Channels

We isolated N-lobe mediated CDI in $Ca_V1.3$ by coexpressing a mutant CaM_{34}, with selective retention of N-lobe Ca^{2+} binding (DeMaria et al., 2001; Yang et al., 2006). In this case, voltage-block yielded $CDI(\infty)$–P_O data (Figures 3H–3K) which formed a shallower, but still local Ca^{2+} profile (Figure 3K), corresponding to an SQS profile with $r = 5.44$ (Equation 2). This outcome suggests that N-lobe mediated regulation of $Ca_V1.3$ may be a natural example where channel affinity for Ca^{2+}/CaM exceeds its affinity for apoCaM ($r > 1$). Indeed, unlike Ca_V2 channels, $Ca_V1.3$ channels contain an additional Ca^{2+}/CaM binding site in their amino terminus, called *NSCaTE* (Dick et al., 2008). As *NSCaTE* only binds Ca^{2+}/CaM but not apoCaM (Supplemental Data [5A]), this added site could increase r, causing a shift to local selectivity.

Full experimental verification of prediction 2 would require incremental adjustments of r, so we scanned the $Ca_V1.3$ *NSCaTE* (Figure 4A, top sequence) for alanine point mutations yielding graded effects on CDI and Ca^{2+}/CaM affinity. The far left data bar reflects the baseline N-lobe CDI (f_{500}) for wild-type $Ca_V1.3$ channels under high buffering. Data bars to the right reveal a reduction in CDI for alanine substitutions at three residues (Figure 4A, top sequence, in bold) with the rank order of reduction: W44A > I48A > R52A. Consistent with expectations of the SQS mechanism, these mutations induced proportional effects on the relative dissociation constant ($K_{d,EFF}$) between Ca^{2+}/CaM and *NSCaTE* (Figure 4B), as measured by live-cell FRET two-hybrid assays (Erickson et al., 2003). Here, EYFP fused to CaM was tested for FRET interaction with ECFP fused to a $Ca_V1.3$ amino-terminal fragment bearing *NSCaTE*. The strong Ca^{2+}/CaM interaction with intact *NSCaTE* (far left bar) was disrupted (heightened $K_{d,EFF}$) by alanine substitution at the same three residues. To more accurately estimate *NSCaTE* affinity for the Ca^{2+}-bound N-lobe, we measured the FRET interaction between Ca^{2+}/CaM_{34} and *NSCaTE* (Figure 4C). Reassuringly, these changes in affinity mirrored more closely the functional alterations of N-lobe CDI (Figure 4A; Supplemental Data [5A]).

We then examined the effects of these mutations on $CDI(\infty)$–P_O behavior, focusing initially on the I48A construct which exhibited weak, but readily measurable N-lobe CDI in high buffering. Single-channel activation was unchanged from wild-type (Supplemental Data [5B]). As well, voltage block of its C-lobe mediated CDI (Figures 4D and 4E) produced data points (panel E, symbols) that were readily fit by the identical $CDI(\infty)$–P_O relation as the wild-type channel (curve). These results emphasize that *NSCaTE* mutations can specifically modulate N-lobe regulation, and confirm that C- and N-lobes trigger genuinely distinct

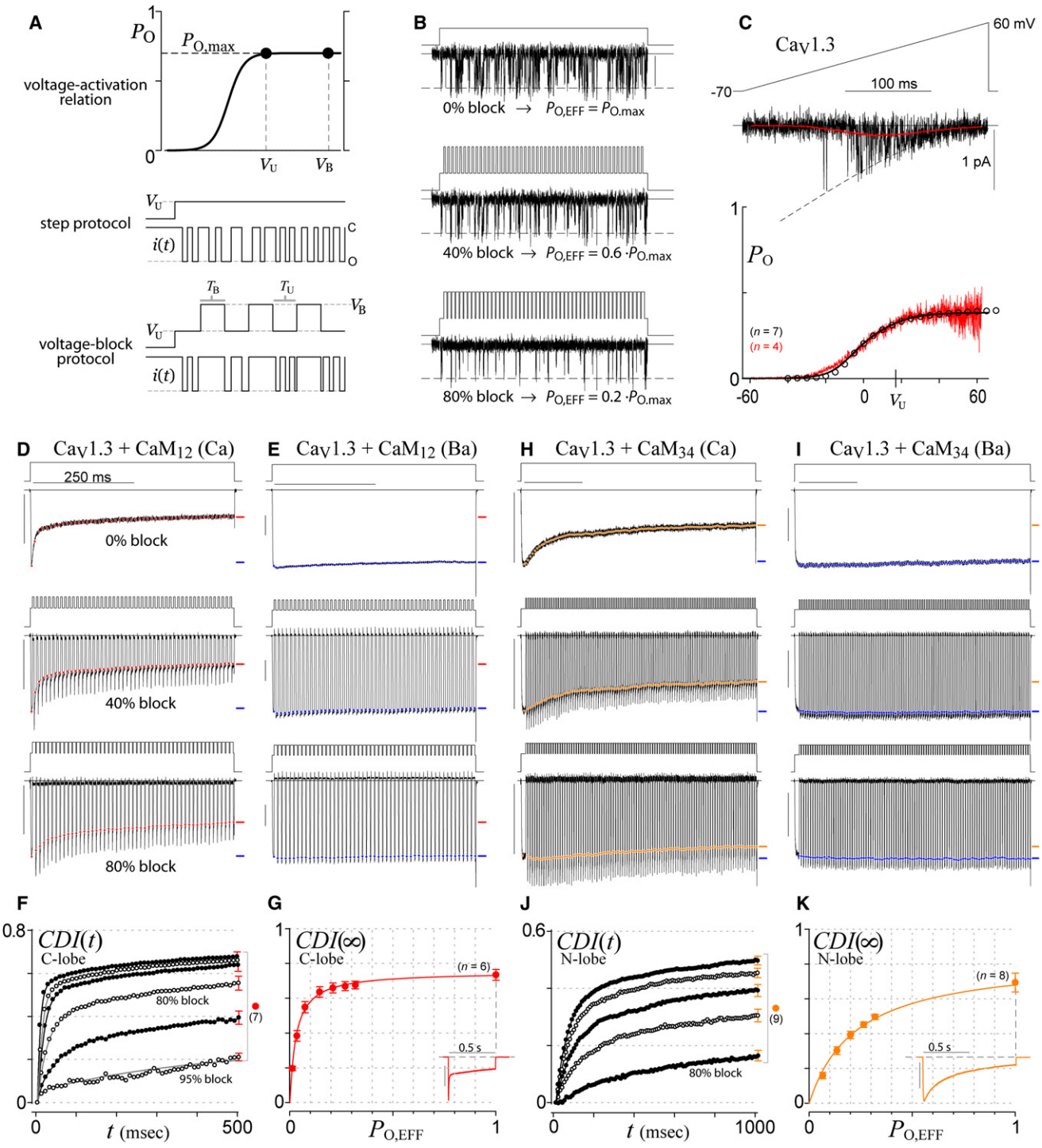

Figure 3. Voltage Block Theory and Experiment

(A) Voltage block theory. Since both V_U and V_B are on the plateau of the voltage-activation relation (top row), the true channel open probability at either voltage is $P_{O,max}$, with channel gating as cartooned in the middle row. By choosing V_B at the reversal potential, sojourns to V_B effectively lower P_O (bottom row).

(B) Schematic of block effects on single $Ca_V1.3$ channel activity (Ba^{2+} currents).

(C) $P_{O,max}$ calibration. Voltage ramps (top) evoked $Ca_V1.3$ single-channel Ba^{2+} records (middle, black trace), which were averaged (middle, red trace), and normalized by the open current level (middle, dashed curve) to yield the voltage-activation relation (bottom, red trace). The whole-cell tail-activation curve (bottom, circles) was scaled in amplitude to match that of the single-channel curve, whereas the whole-cell curve calibrated the single-channel relation along the voltage axis. Cell numbers (*n*) as shown. SEM for whole-cell data was smaller than symbol size. See Supplemental Data (4A and 4B) for details.

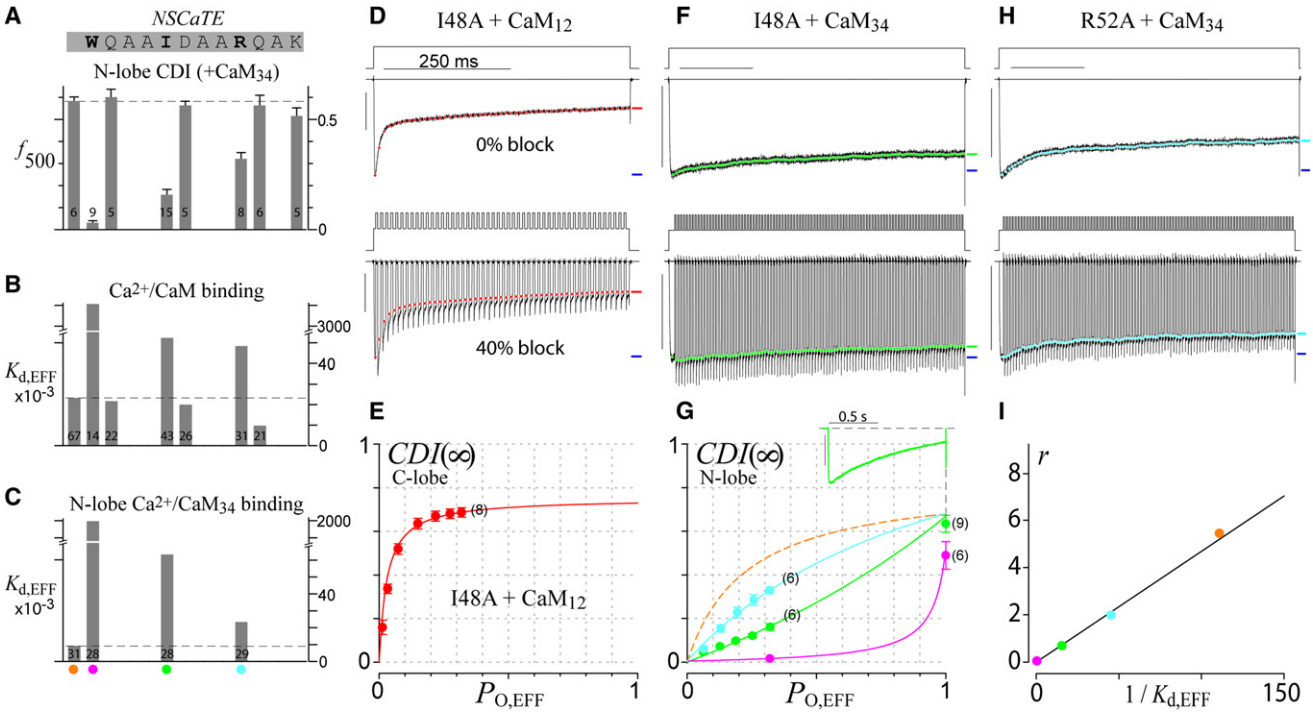

Figure 4. Mutations in *NSCaTE* Transform N-Lobe Spatial Selectivity of $Ca_V1.3$

(A) Scanning alanine mutagenesis of $Ca_V1.3$ *NSCaTE* (top), with corresponding N-lobe CDI (isolated with CaM_{34}) in high buffering (bottom); f_{500} is the difference in fractional Ba^{2+} versus Ca^{2+} currents remaining after 500 ms depolarization. Leftmost bar, wild-type.

(B and C) Effects of alanine mutations on FRET interaction between α_{1D} *NSCaTE* and Ca^{2+}/CaM (B) or Ca^{2+}/CaM_{34} (C). $K_{d,EFF}$ is the effective dissociation constant (Supplemental Data [5A]).

(D and E) Voltage-block of C-lobe CDI for I48A mutant of $Ca_V1.3$ (as in Figures 3D and 3G).

(F–H) Voltage-block of N-lobe CDI for I48A ([F and G] green), and R52A ([G and H] cyan). W44A mutant is coarsely plotted and fit ([G] magenta). Dashed orange curve (G) replicates the native channel relation from Figure 3K.

(I) Correlation between $1/K_{d,EFF}$ from (C) and model parameter *r* from fits in (G). Color schemes as before (orange: wild-type *NSCaTE*; cyan: R52A; green: I48A; magenta: W44A).

Error bars show SEM, with cell numbers (*n*) as shown.

processes. Contrasting with the lack of collateral effects, the N-lobe *CDI*(∞)–P_O relation for I48A was converted into a global relation with apparent upward curvature (Figures 4F and 4G, green), fitting with a diminished $r = 0.69$. The wild-type *NSCaTE* relation (dashed orange) gauges the extent of this conversion. Additionally, the R52A construct yielded an intermediate relation (Figures 4H and 4G, cyan, $r = 1.98$), and W44A produced the most extreme global relation (Figure 4G, magenta, $r = 0.04$). According to the SQS mechanism (Equation 2), *r* should be proportional to channel affinity for the Ca^{2+}-bound N-lobe, assuming channel affinity for apoCaM is held constant. In this regard, *NSCaTE* only binds Ca^{2+}/CaM and not apoCaM (Supplemental Data [5A]), and its amino terminal location is distinct from carboxy-terminal apoCaM binding (Erickson et al., 2003; Pitt et al., 2001). Hence, the parameter *r* should be directly proportional to *NSCaTE* affinity for Ca^{2+}/CaM_{34} ($\propto 1/K_{d,EFF}$ in Figure 4C). The tight linear relation in Figure 4I between electrophysiological determinations of *r* (Figure 4G) and corresponding *NSCaTE* binding affinities for Ca^{2+}/CaM_{34} (Figure 4C) fulfills prediction 2, in support of the SQS mechanism.

High P_O Variant of $Ca_V1.3$ Enables High-Resolution Voltage-Block Analysis

Our high-buffering data have thus far been restricted by the low native $P_{O,max}$ of $Ca_V1.3$ channels (= 0.3), limiting the extent to which *CDI*(∞)–P_O shape can be resolved (prediction 3).

(D and E) Voltage-block traces for $Ca_V1.3$ C-lobe inactivation (isolated with CaM_{12}) in Ca^{2+} (D) and Ba^{2+} (E). Voltage waveforms are above each current trace. Red symbols indicate time course of inactivation during each block cycle (Supplemental Data [4C]). Final extent of inactivation indicated by red (Ca^{2+}) or blue (Ba^{2+}) dash. Scale bars 1 nA, 250 ms, throughout.

(F) Time course of pure CDI (Ca^{2+} inactivation normalized by Ba^{2+} inactivation). SEM is shown for the 500 ms time points, and is similar at other times. From top to bottom: 0%, 40%, 60%, 80%, 90%, and 95% block.

(G) Experimentally determined *CDI*(∞)–P_O relationship, corresponding to 500 ms points in (F). All voltage-block data ($P_O < 1$) obtained under high buffering by 10 mM BAPTA, here and throughout. Inset: Low buffer data in 0.5 EGTA is a lower-limit proxy for $P_O \sim 1$. Error bars show SEM, with cell numbers (*n*) as shown.

(H–K) Voltage block of N-lobe CDI (isolated with CaM_{34}); format as in (D)–(G), except all analysis is done after 1 s. CDI time course (J) for 0%, 20%, 40%, 60%, 80% block (top to bottom). Error bars show SEM, with cell numbers (*n*) as shown.

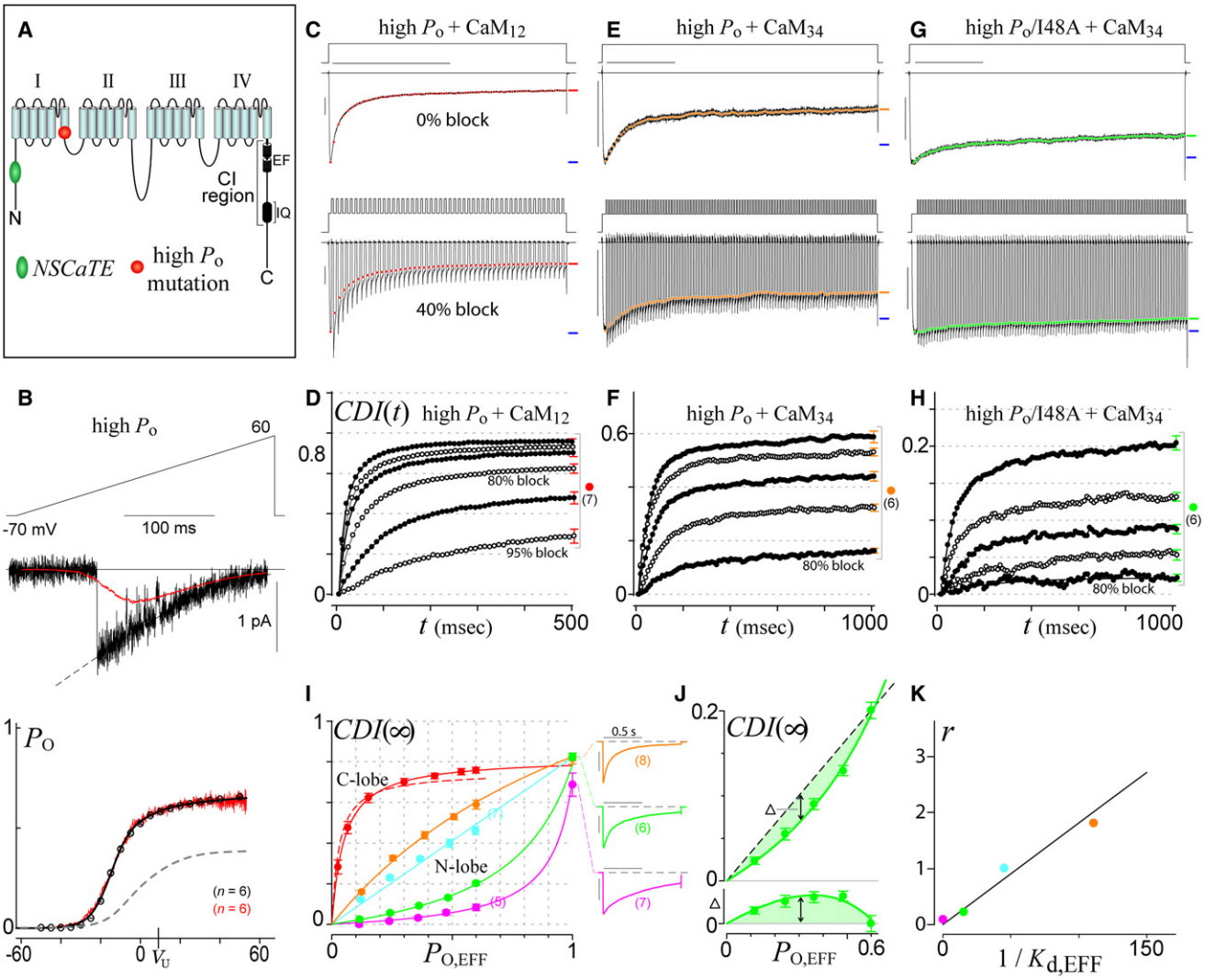

Figure 5. High P_O Variant of $Ca_V1.3$ Enables High-Resolution Voltage-Block Analysis

(A) Cartoon of α_{1D} pore-forming subunit of $Ca_V1.3$, locating *NSCaTE* and high-P_O mutations.

(B) $P_{O,max}$ calibration for high-P_O variant of $Ca_V1.3$ (as in Figure 3C). Dashed curve in bottom graph replicates the native channel relation from Figure 3C.

(C and D) Voltage-block of C-lobe CDI for high-P_O $Ca_V1.3$. Format as in Figures 3D and 3F.

(E–H) Voltage-block of N-lobe CDI for high-P_O $Ca_V1.3$ (E and F) and high-P_O I48A (G and H).

(I) High-P_O $CDI(\infty)$–P_O relationships. Solid red curve corresponds to C-lobe CDI from (D). Dashed red curve replicates the native C-lobe profile from Figure 3G. Other curves correspond to high-P_O N-lobe CDI, with colors as before (orange: wild-type *NSCaTE* from (F); cyan: R52A; green: I48A from (H); magenta: W44A). Low buffer data in 0.5 EGTA (exemplars to right) are lower-limit proxies for $P_O \sim 1$. Error bars show SEM, with cell numbers (n) as shown.

(J) Magnified view of high-P_O I48A profile from (I), showing only high-buffer voltage-block data. Comparison of data to a dashed linear relation (top), with difference between dashed line and data points (bottom), demonstrates clear upward curvature.

(K) Correlation between $1/K_{d,EFF}$ from Figure 4C and model parameter r from fits in (I).

Extensive mutagenesis revealed an L396P point mutation in $Ca_V1.3$ (Figure 5A) that considerably hyperpolarizes activation and doubles $P_{O,max}$ (= 0.6, Figure 5B). Fortunately, this P_O-enhancing mutation left both forms of CDI largely unchanged. The C-lobe profile for the L396P construct (Figures 5C, 5D, and 5I, solid red curve) was indistinguishable from the saturating wild-type relation (Figure 5I, dashed red curve), in further support of prediction 1. As well, the N-lobe behavior was mostly unperturbed (Figures 5E, 5F, and 5I, orange, r = 1.8). Against this high-P_O background, the I48A mutation produced a well-resolved global profile with r = 0.21 (Figures 5G, 5H, and 5I, green). The stronger W44A mutation showed a more pronounced global profile with smaller r = 0.075 (Figure 5I, magenta; Supplemental Data [5B]), and the mildest R52A manipulation yielded the smallest conversion from local behavior (Figure 5I, cyan, r = 1.0). The linear relation between r and the channel affinity for Ca^{2+}/CaM_{34} (Figure 5K), here obtained from highly-resolved $CDI(\infty)$–P_O data, further validates

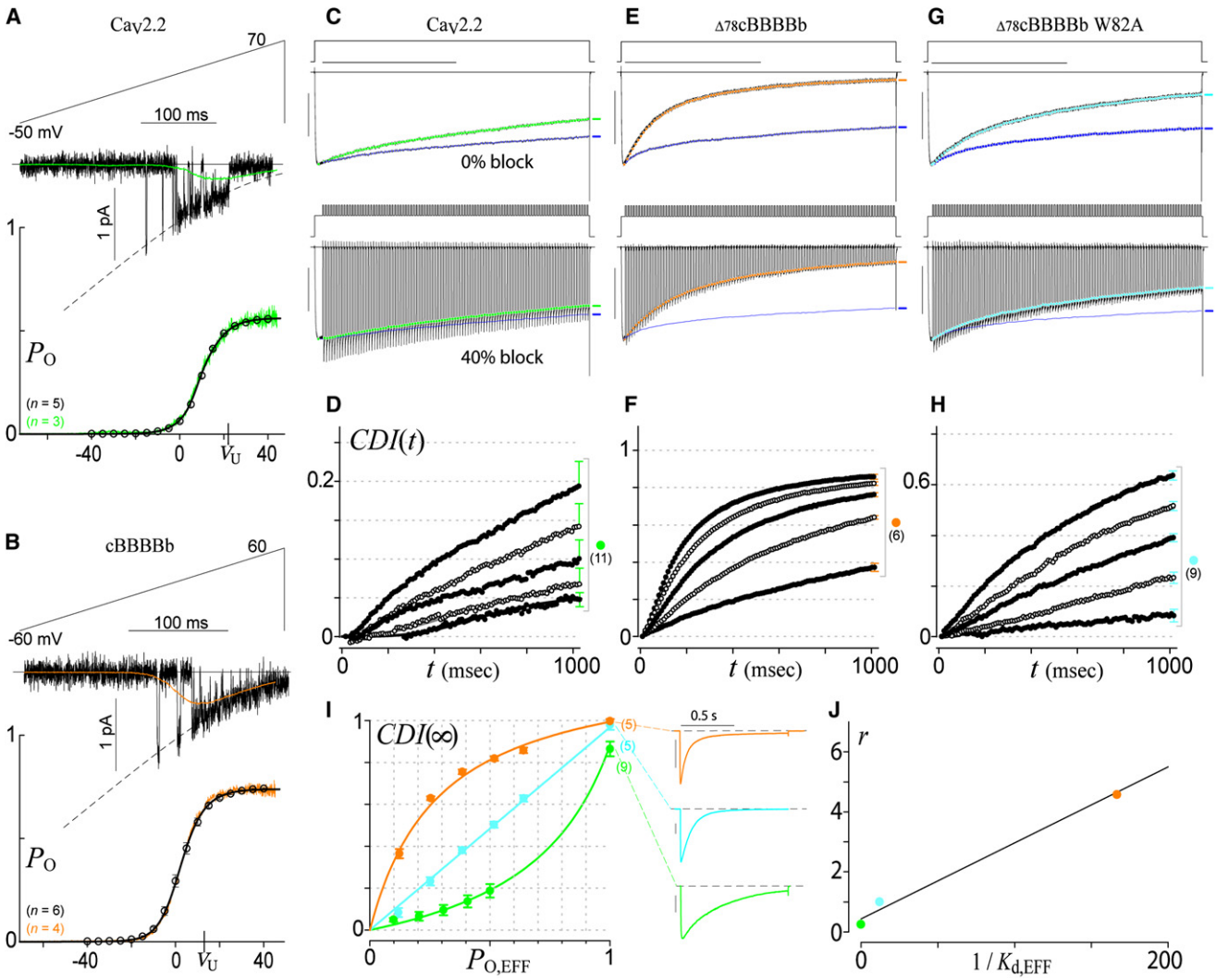

Figure 6. The SQS Mechanism Generalizes to Ca_V2 Channels

(A and B) $P_{O,max}$ calibration for $Ca_V2.2$ (A) and cBBBBb (B). Format as in Figure 3C.

(C–I) Voltage-block analysis of $Ca_V2.2$ ([C, D, and I] green), Δ78cBBBBb ([E, F, and I] orange), and W82A mutant of Δ78cBBBBb ([G–I] cyan). Blue waveforms in (C, E, and G) follow the Ba^{2+} current trajectory (e.g., symbols in Figure 3E) corresponding to the same percentage block. Error bars show SEM, with cell numbers (*n*) as shown.

(J) Correlation between $1/K_{d,EFF}$ from FRET binding of α_{1C} *NSCaTE* with Ca^{2+}/CaM_{34} (Dick et al., 2008) and model parameter *r* from fits in (I).

prediction 2. Furthermore, both the high-P_O I48A and W44A mutants exhibited upward curvature that was clear, even without the estimated $P_O \sim 1$ data. In particular, if the high-buffer I48A data from Figure 5I (green) is compared to a linear profile on an expanded scale (Figure 5J, top), the upward curvature becomes obvious. The undershoot of the data compared to the dashed linear profile is quantified by the difference plot below (Figure 5J, bottom), and the nonlinear fit of the SQS mechanism (green curve) statistically outperforms a linear fit (p = 0.003, *F*-test statistic). Analysis of W44A also indicates significant upward curvature (p = 0.05). These outcomes for high-P_O I48A and W44A constructs thus fulfill prediction 3 (Supplemental Data [4E]). In sum, these high-P_O data fully satisfy all predictions of the slow CaM (C-lobe) and SQS (N-lobe) mechanisms.

Generalization of the SQS Ca^{2+}-Sensing Mechanism to $Ca_V2.2$ Channels

We next tested if the SQS mechanism could apply more generally and explain the well-known global Ca^{2+} selectivity of N-lobe mediated CDI in Ca_V2 channels (Evans and Zamponi, 2006; Liang et al., 2003). According to this mechanism, the global selectivity of Ca_V2 would arise from the lack of an intrinsic *NSCaTE*, rendering these channels the natural equivalent of $Ca_V1.3$ *NSCaTE* mutants. Fitting with this view, the inclusion of *NSCaTE* within the amino terminus of $Ca_V2.2$ channels renders their N-lobe CDI insensitive to high Ca^{2+} buffering (Dick et al., 2008). To test the SQS mechanism in $Ca_V2.2$, we calibrated $P_{O,max}$ (Figure 6A), and performed voltage-block experiments that confirmed a global $CDI(\infty)$–P_O relation with $r = 0.25$ (Figures 6C,

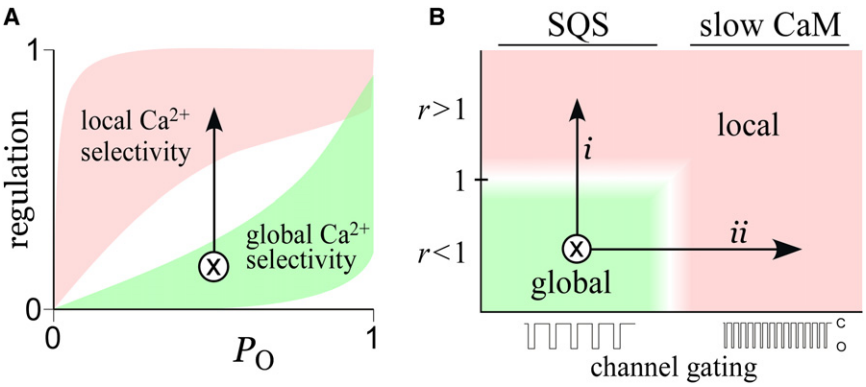

Figure 7. Physiological Modulation of the SQS Mechanism

(A) Graphical depiction of transformation from global to local selectivity.

(B) Physiologically plausible mechanisms of spatial selectivity transformation. The vertical axis shows *r*, the ratio of channel affinity for Ca^{2+}/CaM versus apoCaM; and the horizontal axis depicts the speed of channel gating, given fixed CaM kinetics. Transformation from global to local could arise from increasing *r* (trajectory *i*), or by speeding channel gating (trajectory *ii*).

6D, and 6I, green). Substitution of a $Ca_V1.2$ amino terminus containing *NSCaTE* (Δ78cBBBBb) imparted a pronounced conversion to a local saturating relation with $r = 4.6$ (Figures 6B, 6E, 6F, and 6I, orange). Moreover, attenuation of CaM/*NSCaTE* interaction through a W82A mutation (~W44A in $Ca_V1.3$) yielded an intermediate profile with $r = 1.0$ (Figures 6G, 6H, and 6I, cyan). Finally, Figure 6J demonstrates the predicted correlation between $Ca_V1.2$ *NSCaTE* affinities for Ca^{2+}/CaM_{34} (Dick et al., 2008) and $CDI(\infty)$–P_O determinations of *r* (Figure 6I). This array of transformations generalize the SQS mechanism across Ca_V1 and Ca_V2 channels.

DISCUSSION

The tight coupling of Ca^{2+} sensors to Ca^{2+} sources affords rapid and privileged signaling, but requires special sensing capabilities. In the CaM/Ca^{2+}-channel complex, these capabilities are exemplified by the contrasting spatial Ca^{2+} selectivities of the two lobes of CaM. Here, we establish that these selectivities are achieved not by sensing Ca^{2+} in different locations (Figure 1A, top row), but by decoding distinct temporal characteristics of nanodomain Ca^{2+} (bottom row). Local selectivity of the C-lobe arises from a slow CaM mechanism that exploits channel proximity and responds to intense yet intermittent Ca^{2+} signals. This local selectivity mechanism likely pertains to all forms of C-lobe regulation of Ca^{2+} channels, including the Ca^{2+}-dependent facilitation (instead of CDI) of $Ca_V2.1$ channels (DeMaria et al., 2001). Conversely, global selectivity of the N-lobe disregards local signals and responds to weaker Ca^{2+} signals from distant sources. This vital capability arises from an SQS mechanism highly attuned to the fractional presence, but not intensity of signals. This mechanism also explains the switching of N-lobe selectivity between global (Ca_V2) and local (Ca_V1) extremes (Dick et al., 2008).

Validity and Uniqueness of the SQS Mechanism of Ca^{2+} Sensing

The arguments for the SQS mechanism warrant special emphasis. For prediction 2, the parameter *r* is drawn from fits of Equation 2 to data that are highly constrained (Supplemental Data [4D]). Thus, a key aspect of this prediction—the linear correlation between *r* and CaM/*NSCaTE* binding affinity (e.g., Figure 5K)—is well satisfied. For prediction 3, upward curvature of $CDI(\infty)$–P_O relations not only supports validity, but also the uniqueness of the SQS mechanism. For the four-state configuration (Figure 2A), moderate kinetic deviations from the SQS regime (e.g., slowing Ca^{2+}/CaM interactions, speeding channel/CaM interactions) always diminish the upward curvature of $CDI(\infty)$–P_O relations, and larger deviations altogether preclude such curvature (Supplemental Data [1B–1E]). Thus, the SQS mechanism embodies the core principles by which any four-state mechanism can produce upward curvature. Moreover, if other states are included (Ca^{2+}/CaM binding to the apoCaM site, apoCaM binding to the Ca^{2+}/CaM site), upward curvature is only achieved insofar as these extra states are rarely occupied (Supplemental Data [1F]). Hence, the upward curvature seen in four constructs (Figure 5J, Supplemental Data [4E]) argues most strongly for the SQS mechanism.

Methodology for Investigating Ca^{2+} Sensing within Intact Signaling Complexes

Ca^{2+} decoding often entails multiple CaM/protein interactions whose function may not be apparent when taken out of context. Hence, successful mechanistic dissection may require experimental tools tailored to the intact signaling complex. Here, this is achieved by voltage block of high-P_O channels, which affords millisecond control of nanodomain Ca^{2+} signals of intact channels. Voltage block may be adapted to other Ca^{2+}-permeable channels (Bradley et al., 2004; Myers and Julius, 2007; Saimi and Kung, 2002; Xiong et al., 2002; Zhang and Huganir, 1999), which may well use SQS-like mechanisms, given the prevalence of apoCaM interaction and rapid Ca^{2+} release from CaM. The technique could also extend to sensors that do not regulate ionic current (Jurado et al., 1999), if the Ca^{2+}-regulated molecule is engineered for optical readouts (Takao et al., 2005). For example, this approach could be applied to activity-dependent signaling that triggers nuclear transcription (Cullen, 2006; Oliveria et al., 2007; Winslow and Crabtree, 2005).

Potential Physiological Modulation of Spatial Selectivity

The SQS mechanism suggests how spatial Ca^{2+} selectivity could be physiologically modulated. Figure 7A reviews our graphical definitions of spatial Ca^{2+} sensing, where the black arrow indicates a generic transformation from global (green shaded area) to local (red area) selectivity. There are two main scenarios for such transformation, as developed in Figure 7B. Here, the rectangular green area signifies global selectivity, which only occurs when CaM kinetics are quick relative to channel gating (as in

the SQS mechanism), and when apoCaM affinity exceeds Ca^{2+}/CaM affinity ($r < 1$). Accordingly, trajectory *i* denotes one means of global-to-local transformation, involving an increase in *r*. This could result from physiological modulation of Ca^{2+}/CaM and/or apoCaM interaction sites; for example by phosphorylation (De Koninck and Schulman, 1998) or by competition with phospholipids and ATP (Myers and Julius, 2007). A second means of transformation exploits the fact that "slow" and "quick" binding interactions are defined relative to gating. Hence, accelerating gating, while holding CaM binding dynamics fixed (Figure 7B, trajectory *ii*), could induce deviations from global SQS behavior to a local, slow CaM profile. In heart failure, for example, ryanodine receptor closed times are dramatically shortened (Marx et al., 2000), potentially promoting local selectivity and long-range signaling deficits. In all, this study elucidates the mechanism of Ca^{2+} decoding by the CaM/channel complex, suggests how this sensing can be physiologically tuned, and expands our understanding of the Ca^{2+} signaling "toolkit" (Bootman et al., 2001) prevalent throughout biology.

EXPERIMENTAL PROCEDURES

Numerical Simulations

Numerical simulations (Figures 2C and 2G) were performed in MATLAB (MathWorks, Natick, MA), as detailed in Supplemental Data (4F). Additional numerical simulations, including those demonstrating the equivalence of continuum and stochastic views of nanodomain Ca^{2+} decoding, are elaborated in Supplemental Data (1–3).

Molecular Biology

Point mutations of $Ca_V1.3$ (α_{1D}) *NSCaTE* (Figure 4) were made in rat α_{1D} (Xu and Lipscombe, 2001). A 600 bp stretch containing *NSCaTE* (bounded by NheI and BsiWI) was cloned into Zero Blunt TOPO (Invitrogen), yielding NT_D-TOPO. QuikChange (Stratagene) was used to mutate *NSCaTE* within NT_D-TOPO, and the relevant region was transferred into α_{1D} by NheI/BsiWI sites. The high-P_O $Ca_V1.3$ (Figure 5) was similarly constructed via a 2.3 kb stretch bounded by BsiWI and Eco47III. $\alpha_{1cBBBBb}$, $\alpha_{1c78BBBBb}$ and $\alpha_{1c78BBBBb}$ W82A were as described (Dick et al., 2008). CFP-NT_D was made by PCR of α_{1D} *NSCaTE* residues 35–94, as present within NT_D-TOPO (± mutations), followed by substitution for CaM_{WT} in CFP-CaM_{WT}/pcDNA3 (Erickson et al., 2003) via NotI/XbaI. All segments subject to PCR were verified by sequencing.

Transfection of HEK293 Cells

For electrophysiology, HEK293 cells were cultured on 10 cm plates, and transiently transfected by a calcium phosphate protocol (Peterson et al., 1999). We combined 8 μg each of cDNAs encoding channel α_1 subunit, rat brain β_{2a} (Perez-Reyes et al., 1992), rat brain $\alpha_{2\delta}$ (Tomlinson et al., 1993), and rat brain CaM_{12} or CaM_{34} (Peterson et al., 1999), along with 1-2 μg of SV40 T antigen. All subunits were driven by a CMV promoter. Experiments were done 1–2 days later.

FRET Two-Hybrid Assay

FRET two-hybrid was performed as described (Erickson et al., 2003) (Supplemental Data [5A]). Experiments were carried out in a 10 mM Ca^{2+} Tyrode's buffer with 10 μM ionomycin (Sigma-Aldrich, MO) added for all Ca^{2+}/CaM conditions.

Whole-Cell Electrophysiology

Whole-cell recordings were obtained at room temperature (Axopatch 200A, Axon Instruments). Electrodes were pulled borosilicate glass capillaries (World Precision Instruments, MTW 150-F4), with 1–3 MΩ resistances, before 80% series resistance compensation. Currents were filtered at 2 kHz for routine rectangular steps, and 5 kHz for voltage-block and tail-activation (4-pole Bessel). A P/8 leak-subtraction protocol was used. For all voltage-block, tail-activation, and high-buffer-CDI experiments, the internal solution contained (in mM): $CsMeSO_3$, 114; $CsCl_2$, 5; $MgCl_2$, 1; MgATP, 4; HEPES (pH 7.4), 10; and BAPTA, 10; at 295 mOsm adjusted with $CsMeSO_3$. For physiological buffering experiments, 135 mM $CsMeSO_3$ and 0.5 mM EGTA were used. For whole-cell experiments based on $Ca_V1.3$ (Figures 3–5), external solutions contained (in mM): TEA-$MeSO_3$, 102; HEPES (pH 7.4), 10; and $CaCl_2$ or $BaCl_2$, 40; at 300 mOsm, adjusted with TEA-$MeSO_3$. For $Ca_V2.2$ (Figure 6), 5 mM $BaCl_2$ or $CaCl_2$ and 140 mM TEA-$MeSO_3$ were used. Further details in Supplemental Data (4B and 4C).

Single-Channel Recordings

On-cell recordings were obtained at room temperature (integrating mode, Axopatch 200B; Axon Instruments). Patch pipettes (5–20 MΩ) were pulled from ultra-thick-walled borosilicate glass (BF200-116-10, Sutter Instruments), and coated with Sylgard. Currents were filtered at 2 kHz. To zero membrane potential, the bath contained (in mM): K glutamate, 132; KCl, 5; NaCl, 5; MgCl, 3; EGTA, 2, glucose, 10; and HEPES (pH 7.4), 20 at 300 mOsm adjusted with glucose. The pipette solution for $Ca_V1.3$ was the same as the Ba^{2+} bath solution in whole-cell experiments. The $Ca_V2.2$ pipette solution contained (in mM): TEA-$MeSO_3$, 20; HEPES (pH 7.4), 10; and $BaCl_2$, 90; at 300 mOsm, adjusted with TEA-$MeSO_3$. Further details in Supplemental Data (4A).

SUPPLEMENTAL DATA

Supplemental Data include Supplemental Experimental Procedures, nineteen figures, three tables, one movie, and Supplemental References and can be found with this article online at http://www.cell.com/cgi/content/full/133/7/1228/DC1/.

ACKNOWLEDGMENTS

We thank Wanjun Yang for dedicated technical support; Michael Caterina, King-Wai Yau, Eric Young, Henry Colecraft, Josh Vogelstein, and members of CSL for helpful feedback on the manuscript; and Will Grimes and Jeffrey Diamond for assistance with MCell. Supported by grants from NIGMS (to M.R.T.), NINDS (to I.E.D.), and from NIMH and NHLBI (to D.T.Y.). Author contributions are as follows: M.R.T. contributed the theoretical insights, computational modeling, and data analysis methodology (Supplemental Data [1–4]) and performed the voltage-block experiments. I.E.D. identified the *NSCaTE* motif, performed single-channel experiments, and FRET-two-hybrid binding assays. D.T.Y. conceived of voltage block, contributed to formalizing the theory, and provided overall guidance and support. All three authors made unique and significant contributions to this work.

Received: September 21, 2007
Revised: February 22, 2008
Accepted: May 16, 2008
Published: June 26, 2008

REFERENCES

Augustine, G.J., Santamaria, F., and Tanaka, K. (2003). Local calcium signaling in neurons. Neuron *40*, 331–346.

Bayley, P., Ahlstrom, P., Martin, S.R., and Forsen, S. (1984). The kinetics of calcium binding to calmodulin: Quin 2 and ANS stopped-flow fluorescence studies. Biochem. Biophys. Res. Commun. *120*, 185–191.

Berridge, M.J., Lipp, P., and Bootman, M.D. (2000). The versatility and universality of calcium signalling. Nat. Rev. Mol. Cell Biol. *1*, 11–21.

Black, D.J., Halling, D.B., Mandich, D.V., Pedersen, S.E., Altschuld, R.A., and Hamilton, S.L. (2005). Calmodulin interactions with IQ peptides from voltage-dependent calcium channels. Am. J. Physiol. Cell Physiol. *288*, C669–C676.

Bootman, M.D., Lipp, P., and Berridge, M.J. (2001). The organisation and functions of local Ca(2+) signals. J. Cell Sci. *114*, 2213–2222.

Bradley, J., Bonigk, W., Yau, K.W., and Frings, S. (2004). Calmodulin permanently associates with rat olfactory CNG channels under native conditions. Nat. Neurosci. *7*, 705–710.

Catterall, W.A. (1999). Interactions of presynaptic Ca2+ channels and snare proteins in neurotransmitter release. Ann. N Y Acad. Sci. *868*, 144–159.

Chaudhuri, D., Alseikhan, B.A., Chang, S.Y., Soong, T.W., and Yue, D.T. (2005). Developmental activation of calmodulin-dependent facilitation of cerebellar P-type Ca2+ current. J. Neurosci. *25*, 8282–8294.

Chaudhuri, D., Issa, J.B., and Yue, D.T. (2007). Elementary Mechanisms Producing Facilitation of Cav2.1 (P/Q-type) Channels. J. Gen. Physiol. *129*, 385–401.

Cullen, P.J. (2006). Decoding complex Ca2+ signals through the modulation of Ras signaling. Curr. Opin. Cell Biol. *18*, 157–161.

De Koninck, P., and Schulman, H. (1998). Sensitivity of CaM kinase II to the frequency of Ca2+ oscillations. Science *279*, 227–230.

DeMaria, C.D., Soong, T.W., Alseikhan, B.A., Alvania, R.S., and Yue, D.T. (2001). Calmodulin bifurcates the local Ca2+ signal that modulates P/Q-type Ca2+ channels. Nature *411*, 484–489.

Dick, I.E., Tadross, M.R., Liang, H., Tay, L.H., Yang, W., and Yue, D.T. (2008). A modular switch for spatial Ca^{2+} selectivity in the calmodulin regulation of Ca_V channels. Nature *451*, 830–834.

Dolmetsch, R.E., Xu, K., and Lewis, R.S. (1998). Calcium oscillations increase the efficiency and specificity of gene expression. Nature *392*, 933–936.

Dunlap, K. (2007). Calcium channels are models of self-control. J. Gen. Physiol. *129*, 379–383.

Erickson, M.G., Alseikhan, B.A., Peterson, B.Z., and Yue, D.T. (2001). Preassociation of calmodulin with voltage-gated Ca(2+) channels revealed by FRET in single living cells. Neuron *31*, 973–985.

Erickson, M.G., Liang, H., Mori, M.X., and Yue, D.T. (2003). FRET two-hybrid mapping reveals function and location of L-type Ca2+ channel CaM preassociation. Neuron *39*, 97–107.

Evans, R.M., and Zamponi, G.W. (2006). Presynaptic Ca2+ channels–integration centers for neuronal signaling pathways. Trends Neurosci. *29*, 617–624.

Gu, X., and Spitzer, N.C. (1995). Distinct aspects of neuronal differentiation encoded by frequency of spontaneous Ca2+ transients. Nature *375*, 784–787.

Houdusse, A., Gaucher, J.F., Krementsova, E., Mui, S., Trybus, K.M., and Cohen, C. (2006). Crystal structure of apo-calmodulin bound to the first two IQ motifs of myosin V reveals essential recognition features. Proc. Natl. Acad. Sci. USA *103*, 19326–19331.

Imredy, J.P., and Yue, D.T. (1994). Mechanism of Ca^{2+}-sensitive inactivation of L-type Ca^{2+} channels. Neuron *12*, 1301–1318.

Jurado, L.A., Chockalingam, P.S., and Jarrett, H.W. (1999). Apocalmodulin. Physiol. Rev. *79*, 661–682.

Li, W., Llopis, J., Whitney, M., Zlokarnik, G., and Tsien, R.Y. (1998). Cell-permeant caged InsP3 ester shows that Ca2+ spike frequency can optimize gene expression. Nature *392*, 936–941.

Liang, H., DeMaria, C.D., Erickson, M.G., Mori, M.X., Alseikhan, B.A., and Yue, D.T. (2003). Unified mechanisms of Ca2+ regulation across the Ca2+ channel family. Neuron *39*, 951–960.

Linse, S., Helmersson, A., and Forsen, S. (1991). Calcium binding to calmodulin and its globular domains. J. Biol. Chem. *266*, 8050–8054.

Martin, S.R., Andersson Teleman, A., Bayley, P.M., Drakenberg, T., and Forsen, S. (1985). Kinetics of calcium dissociation from calmodulin and its tryptic fragments. A stopped-flow fluorescence study using Quin 2 reveals a two-domain structure. Eur. J. Biochem. *151*, 543–550.

Marx, S.O., Reiken, S., Hisamatsu, Y., Jayaraman, T., Burkhoff, D., Rosemblit, N., and Marks, A.R. (2000). PKA phosphorylation dissociates FKBP12.6 from the calcium release channel (ryanodine receptor): defective regulation in failing hearts. Cell *101*, 365–376.

Mori, M.X., Erickson, M.G., and Yue, D.T. (2004). Functional stoichiometry and local enrichment of calmodulin interacting with Ca2+ channels. Science *304*, 432–435.

Myers, B.R., and Julius, D. (2007). TRP channel structural biology: new roles for an old fold. Neuron *54*, 847–850.

Naraghi, M., and Neher, E. (1997). Linearized buffered Ca2+ diffusion in microdomains and its implications for calculation of [Ca2+] at the mouth of a calcium channel. J. Neurosci. *17*, 6961–6973.

Neher, E. (1998). Vesicle pools and Ca^{2+} microdomains: new tools for understanding their roles in neurotransmitter release. Neuron *20*, 389–399.

Neher, E., and Steinbach, J.H. (1978). Local anaesthetics transiently block currents through single acetylcholine-receptor channels. J. Physiol. *277*, 153–176.

Oancea, E., and Meyer, T. (1998). Protein kinase C as a molecular machine for decoding calcium and diacylglycerol signals. Cell *95*, 307–318.

Oliveria, S.F., Dell'Acqua, M.L., and Sather, W.A. (2007). AKAP79/150 anchoring of calcineurin controls neuronal L-type Ca2+ channel activity and nuclear signaling. Neuron *55*, 261–275.

Perez-Reyes, E., Castellano, A., Kim, H.S., Bertrand, P., Baggstrom, E., Lacerda, A.E., Wei, X.Y., and Birnbaumer, L. (1992). Cloning and expression of a cardiac/brain beta subunit of the L- type calcium channel. J. Biol. Chem. *267*, 1792–1797.

Peterson, B.Z., DeMaria, C.D., Adelman, J.P., and Yue, D.T. (1999). Calmodulin is the Ca^{2+} sensor for Ca2+ -dependent inactivation of L- type calcium channels. Neuron *22*, 549–558.

Pitt, G.S., Zuhlke, R.D., Hudmon, A., Schulman, H., Reuter, H., and Tsien, R.W. (2001). Molecular basis of calmodulin tethering and Ca2+-dependent inactivation of L-type Ca2+ channels. J. Biol. Chem. *276*, 30794–30802.

Saimi, Y., and Kung, C. (2002). Calmodulin as an ion channel subunit. Annu. Rev. Physiol. *64*, 289–311.

Schnee, M.E., and Ricci, A.J. (2003). Biophysical and pharmacological characterization of voltage-gated calcium currents in turtle auditory hair cells. J. Physiol. *549*, 697–717.

Sherman, A., Keizer, J., and Rinzel, J. (1990). Domain model for Ca2(+)-inactivation of Ca2+ channels at low channel density. Biophys. J. *58*, 985–995.

Stern, M.D. (1992). Buffering of calcium in the vicinity of a channel pore. Cell Calcium *13*, 183–192.

Stiles, J., and Bartol, T. (2001). Monte Carlo methods for simulating realistic synaptic microphysiology using MCell. In Computational Neuroscience: Realistic Modeling for Experimentalists, E. De Schutter, ed. (Boca Raton, Fla.: CRC Press).

Takao, K., Okamoto, K., Nakagawa, T., Neve, R.L., Nagai, T., Miyawaki, A., Hashikawa, T., Kobayashi, S., and Hayashi, Y. (2005). Visualization of synaptic Ca2+ /calmodulin-dependent protein kinase II activity in living neurons. J. Neurosci. *25*, 3107–3112.

Tomlinson, W.J., Stea, A., Bourinet, E., Charnet, P., Nargeot, J., and Snutch, T.P. (1993). Functional properties of a neuronal class C L-type calcium channel. Neuropharmacology *32*, 1117–1126.

Wang, M.C., Velarde, G., Ford, R.C., Berrow, N.S., Dolphin, A.C., and Kitmitto, A. (2002). 3D structure of the skeletal muscle dihydropyridine receptor. J. Mol. Biol. *323*, 85–98.

Winslow, M.M., and Crabtree, G.R. (2005). Immunology. Decoding calcium signaling. Science *307*, 56–57.

Xiong, L.W., Newman, R.A., Rodney, G.G., Thomas, O., Zhang, J.Z., Persechini, A., Shea, M.A., and Hamilton, S.L. (2002). Lobe-dependent regulation of ryanodine receptor type 1 by calmodulin. J. Biol. Chem. *277*, 40862–40870.

Xu, W., and Lipscombe, D. (2001). Neuronal Ca(V)1.3alpha(1) L-type channels activate at relatively hyperpolarized membrane potentials and are incompletely inhibited by dihydropyridines. J. Neurosci. *21*, 5944–5951.

Yang, P.S., Alseikhan, B.A., Hiel, H., Grant, L., Mori, M.X., Yang, W., Fuchs, P.A., and Yue, D.T. (2006). Switching of Ca2+-dependent inactivation of Ca(v)1.3 channels by calcium binding proteins of auditory hair cells. J. Neurosci. *26*, 10677–10689.

Yang, P.S., Mori, M.X., Antony, E.A., Tadross, M.R., and Yue, D.T. (2007). A single calmodulin imparts distinct N- and C-lobe regulatory processes to individual $Ca_V1.3$ channels (abstr.). Biophys. J. *20a* (Supplement), 1669.

Zhang, S., and Huganir, R.L. (1999). Calmodulin modification of NMDA receptors. Methods Mol. Biol. *128*, 103–111.